Proceedings of the 28th IEEE
EMBS Annual International Conference
New York City, USA, Aug 30-Sept 3, 2006

The Effect of a Distributed Mass Loading on the Frequency Response of a MEMS Mesh Resonator

M.J. Bartkovsky[†], A. Liao[*], G.K. Fedder[*], T.M. Przybycien[†‡], and S. Hauan[†‡]

Abstract— **This paper reports on the development of an acoustic-wave biosensor based on integrated MEMS technology that promises high sensitivity and selectively without the need for molecular tagging or external optical equipment. The device works by detecting frequency shifts resulting from the selective binding of target molecules to the surface of a functionalized resonating polymer MEMS-composite membrane. Here, we characterize the frequency response of our metal-oxide MEMS resonators. We show that the structural topology, which includes the amount of void area spacing, total mass of the resonator, and how the mass is distributed on the surface, affects the resonant frequency response in a measurable way. Using a multimodal electrostatic drive, we can either excite or suppress higher order harmonic frequencies. The excitation of higher order harmonics is important for multiple analyte detection or redundancy testing. We use a finite element model to demonstrate how a distributed mass loading affect the frequency responses of our MEMS structures.**

I. Introduction

Recently, macroscopic quartz crystal resonators and microcantilevers have been used to detect various proteins, antibodies, cells and DNA molecules [1], [3], [8]. The gravimetric detection of target analyte molecules works by monitoring the frequency shifts associated with specific mass adsorption to a surface [5]. Our MEMS-based acoustic-wave sensor promises to be several orders of magnitude more sensitive than these devices due to its larger surface area to mass ratio. Our device consists of a 4x4 array of metal-oxide composite mesh structures suspended over a etched cavity [6]. As opposed to using bulk silicon microfabrication techniques, our MEMS device is based on the design and fabrication of an integrated complementary metal oxide semiconductor (CMOS) chip and post-processing these existing layers with compatible micromachining techniques developed by Fedder, et. al [4]. Adaptation from a MEMS resonator to a biosensing device includes: (a) outfitting the MEMS transducer with sensing elements; in our case the use of embedded piezoresistors on the perimeter of mesh surface, (b) the modification of the metal oxide mesh with a conformal coating of polystyrene, (c) the photochemical functionalization of the polymer surface with immobilized biotin moieties capable of exploiting ligand-ligate specificity, (d) and the incorporation of a clam-shell reservoir for introduction of liquid phase samples to the membrane surface.

[†] Department of Chemical Engineering, [‡] Department of Biomedical Engineering, [*] Department of Electrical and Computer Engineering and The Robotics Institute, Carnegie Mellon University, Pittsburgh, PA 15213 USA

Electronic mail: mbartkov@andrew.cmu.edu (M.J. Bartkovsky)

In this paper, we characterize the frequency response of our metal-oxide mesh structures. Our MEMS chip consists of two different structural mesh designs, a brick mesh and a grid mesh. They differ in both their masses and void areas. Table I summarizes the masses and void spacings for each of the mesh designs. The D mesh structures differ slightly from the other structures in the structural topology of the spatial patterning of metal and oxide on the mesh surface. These slightly variations must be taken into consideration when analyzing the frequency response of each structure.

	Brick A,B,C	**Brick D**	**Grid A,B,C**	**Grid D**
Total Mass	56.49 ng	56.78 ng	80.47 ng	80.42 ng
Void Area	49.5%	49.5%	28.6%	28.7%

TABLE I

TOTAL MASS AND VOID SPACING FOR THE DIFFERENT MESH DESIGNS.

Each mesh structure is individually addressable and can be electrostatically driven at resonance by applied a voltage between the composite metal oxide mesh and the underlying silicon substrate. Each mesh is electrically isolated into four quadrants; thus we can drive them in a monopole, dipole, or quadrupole mode depending upon the orientation of the applied voltage signal to the mesh structure. The ability to preferentially actuate the mesh structures at higher harmonic frequencies is advantageous for a number of reasons. Through simulations [10], we show that the sensitivity of the mesh response is dependent upon the spatial location of mass loading on the surface of the mesh. The largest frequency shifts occur when mass is loaded on the anti-nodes or positions on the mesh surface which experience the maximum displacement. Through monitoring multiple harmonics frequencies, we envision membrane array designs where we can distinguish between more than one target molecule.

II. Materials and Methods

The dynamic response of the mesh structures is measured using a Laser Doppler Vibrometer (LDV). The LDV measures out-of-plane velocities by interferometrically measuring the Doppler-shifted wavelength of the light reflected from a surface. We use an imaging LDV system to continuously scan the surface of the mesh structures. We perform the scanning LDV measurements using a Polytec [7] MSA-400 Microsystem Analyzer. Using a 50x objective, we are able focus a laser spot size down to approximately 1 μm in diameter. Integrated electrical equipment enable us to drive our mesh structures with two out-of-phase pseudo random voltage signals. The applied voltage signals consist of a 4 V

DC offset and a 4 V AC component. The DC offset is used to statically deflect the mesh structure downward towards the underlying silicon substrate. The overlaid AC voltage signal is used to oscillate the mesh structure. We electrostatically drive the mesh structures in either a monopole, dipole, or quadrupole mode depending upon the orientation of the applied voltage signals to the different quadrants on the mesh structures. The scanning LDV measurement allows multiple single-point measurements to be performed producing a three dimensional image of the mesh structure's out-of-plane vibration behavior and frequency response. The complex averaging of each single-point measurement is done on the real and imaginary components individually, so that both the amplitude and the phase information is retained.

III. Results and Discussion

We first excite the brick A mesh structure with a monopole drive whereby the same voltage signal is applied to the entire mesh structure. The resulting frequency response is plotted in Figure 1.

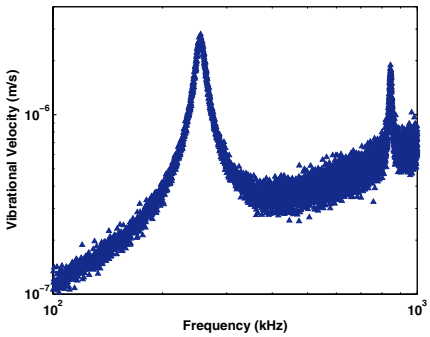

Fig. 1. The brick A mesh is excited with a monopole pseudo random drive voltage. Electrostatically actuating the mesh in a monopolar mode stimulates a resonant peak at 254.3 kHz and another peak at 845.7 kHz.

Scanning the mesh structure allows us to capture a three-dimensional image of the deflection profile at both resonant peaks. The 254.3 kHz resonance corresponds to the (1,1) mode. The (1,1) mode shape is the fundamental mode where the the entire structure moves in phase and the maximum displacement is in the center of the mesh. Using the imaging LDV, we determined that the 845.7 kHz resonance corresponds to the (1,3)+(3,1) mode. This mode shape also has its maximum displacement in the center of the mesh. The static deflection profile for this mode is shown in Figure 2.

The reason we see the additive effect of the (1,3) mode plus the (3,1) mode is because of the method we chose to actuate the mesh structure. The same electrostatic force is applied equally and uniformly to the metal mesh; a monopole excitation method. The monopole excitation damps the other higher order harmonic modes. When a uniform force is applied to the mesh structure, the energy supplied to the system is not sufficient enough to excite some of these other modes.

Characterization experiments are then performed whereby the brick A, B, and C meshes and the grid A, B, and C

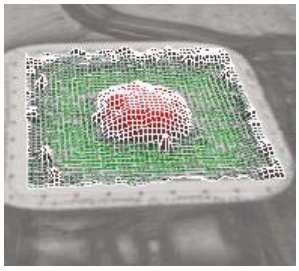

Fig. 2. The measured resonant frequency at 845.7 kHz is a combination of the (1,3)+(3,1) mode. The displacement magnitude for this mode shape is approximately $\pm$ 10 pm at the center.

meshes are driven with a dipole pseudo random voltage signal. Here, out-of-phase voltage signals are applied to opposite halves of each mesh structure. We also use a quadrupole configuration to actuate the brick D and grid D mesh structures. Here, out-of-phase voltage signals are applied to the diagonal quadrants on the mesh structure. The averaged frequency response of the brick A, B, and C meshes and the brick D mesh are depicted in Figure 3. The results from actuating the grid A, B and C mesh structures in a dipole and the grid D mesh structure in a quadrupole mode are depicted in Figure 4.

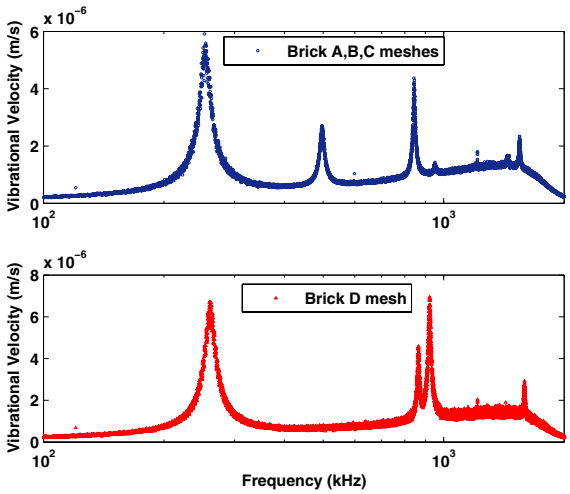

Fig. 3. Applying a dipole drive voltage allows us to excite six resonant frequencies in the brick A, B, and C meshes; the (1,1) mode at 254.3 kHz, the (1,2) mode at 496.4 kHz, the (1,3)+(3,1) mode at 845.7 kHz, the (1,3)-(3,1) mode at 950.3 kHz, the (2,3) mode at 1.45 MHz and the (3,3) mode at 1.55 MHz. Applying the quadrupole drive allows us to excite four resonant frequencies in the brick D mesh; the (1,1) mode at 261.1 kHz, the (1,3)+(3,1) mode at 863.5 kHz, the (2,2) mode at 917.6 kHz, and the (3,3) mode at 1.59 MHz.

Driving the mesh structures in either a dipole or a quadrupole mode allows us to stimulate multiple harmonic frequencies. Depending upon the mode of excitation, we are able to suppress some frequency modes. When we electrostatically drive the mesh structures in a monopole mode, we suppress the excitation of the (1,2) and (2,2) modes. However, when we drive the mesh structures in a

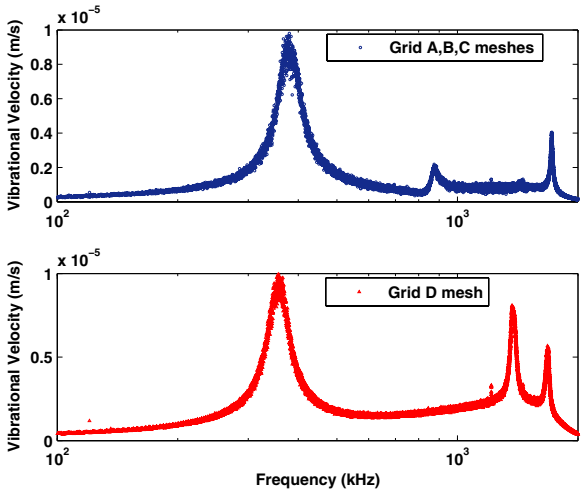

Fig. 4. Applying a dipole drive voltage allows us to excite three resonant frequencies in the grid A, B, and C meshes; the (1,1) mode at 386.2 kHz, the (1,2) mode at 882.8 kHz, the (1,3)+(3,1) mode at 1.71 MHz. Applying the quadrupole drive voltage allows us to excite three resonant frequencies in the Grid D mesh; the (1,1) mode at 355.0 kHz, the (2,2) mode at 1.38 MHz, and the (1,3)+(3,1) mode at 1.68 MHz.

dipole mode, we only suppress the excitation of the (2,2) frequency mode. The brick A, B, and C mesh structures and the grid A, B, and C mesh structures are all identical in their structural topology and total mass; hence they should resonant at the same frequencies. The brick D and grid D structures differ from the other structures in their spatial location of mass on the surface.

Table II summarizes the measured modes, resonant frequencies, and Q-factors for the brick and grid mesh structures. The Q-factors are calculated as the measured resonant frequency divided by the bandwidth, where the bandwidth is defined at the 3 decibel change in intensity from the resonant peak value.

	Brick A, B, and C		Brick D	
Mode	**f [kHz]**	**Q-factor**	**f [kHz]**	**Q-factor**
(1,1)	254.3 ± 0.7	28	261.1 ± 1.2	25
(1,2)	496.4 ± 1.5	41		
(1,3)+(3,1)	845.41 ±	82	863.5 ± 2.8	91
(2,2)			917.6 ± 6.2	74
(1,3)-(3,1)	950.03 ± 0.4	22		
(2,3)	1453.3 ± 8.4	< 10		
(3,3)	1547.9 ± 3.0	101	1592.2 ± 4.2	150
	Grid A, B, and C		**Grid D**	
Mode	**f [kHz]**	**Q-factor**	**f [kHz]**	**Q-factor**
(1,1)	386.2 ± 10.4	12	355.0 ± 8.8	11
(1,2)	882.8 ± 8.6	35		
(2,2)			1378.9 ± 13.6	22
(1,3)+(3,1)	1710.1 ± 19.5	102	1677.2 ± 12.8	47

TABLE II
MEASURED RESONANT FREQUENCIES AND Q-FACTORS FOR BOTH BRICK MESH AND GRID DESIGNS.

We notice the very low standard deviation from structure-to-structure indicating the reliability and reproducibility of the fabrication process. The brick and grid mesh structures which differ in their void area spacing and masses also have different frequency responses. The measured Q-factors for all mesh are between approximately 10 and 150. The Q-factors also increase with increasing resonance. For higher resonant frequencies, the bandwidth is narrower, producing a sharp peak with a higher Q-factor. As the resonant frequency increases, there is less damping in the system. This makes sense since less air is being compressed in the cavity since a portion of the mesh structure is moving out-of-phase.

IV. Modeling the Dynamics of the MEMS Structures

To understand the resonant behavior of our mesh structures, we model the system using the equation of motion for a resonator subjected to an applied electrostatic pressure. We model the mesh structure as a three dimensional plate with elasticity as the restoring force. Plates, unlike membranes, possess bending rigidity as a result of their thickness and elasticity. During transverse vibrations, plates deform primarily by flexing perpendicular to their own plane [2]. The equation of motion used to predict the transverse vibrations of a plate is given by [2]:

$$\frac{Ed^3}{12(1-\nu^2)}\nabla^4 z - P(x,y,t) = \rho d\frac{\partial^2 z}{\partial t^2} \tag{1}$$

where E is the elasticity of the plate, ρ is the density, d is the plate thickness, ν is Poisson's ratio, and P is the applied pressure. The resonant frequencies for a plate with an isotropic elasticity as the restoring force are predicted by [2]:

$$\omega_{om,n} = \frac{\lambda_{m,n}^2}{a}\sqrt{\frac{Ed^3}{12\rho d(1-\nu^2)}} \tag{2}$$

where $\lambda_{m,n}^2$ is dependent upon the boundary conditions along the perimeter of the plate and a is the length of the side of the plate. For a square plate clamped on all four sides, $\lambda_{1,1}^2$ = 35.99, $\lambda_{1,2}^2$ = 73.41, $\lambda_{2,2}^2$ = 108.30, and $\lambda_{1,3}^2$ = 131.60 [2].

The (2,2) mode for a plate with uniform density is at a lower frequency than the degenerate (1,3) and (3,1) modes. However, in the LDV experiments we notice that the (2,2) mode is actually at a higher frequency. We hypothesize that the effect of a distributed mass loading affects the frequency response of our mesh structures. The distributed mass loading stems from the placement of additional metal and oxide layers on the mesh in order to isolate the structure into four individually addressable quadrants. This electrical isolation allows us to drive the meshes in a dipole or quadrupole mode. To test the effect of a distributed mass loading on the surface of our mesh structures, we model the brick D and brick A meshes using a Finite Element Model package, Comsol, Inc. [9], according to Figure 5 and Table III.

The effective plate thickness is calculated using the effective area of the mesh accounting for the void spacings, the thicknesses of each metal and oxide layer comprising the

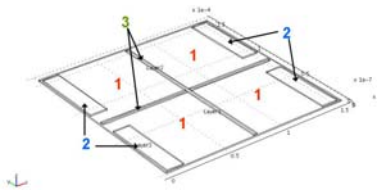

(a)

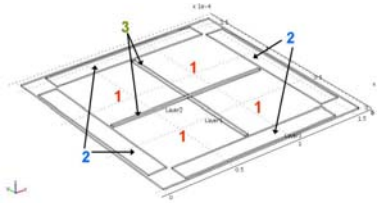

(b)

Fig. 5. FEM geometries used to model the (a) brick D mesh and the (b) brick A mesh. Region 1 is the unloaded portion of the mesh. Region 2 is the additional mass loading needed to isolate the structure into four quadrants. Region 3 is the additional mass loading needed to shield the polysilicon piezoresistors. The additional mass consists of metal and oxide.

	$\mathbf{E}_{eff}$ **GPa**	$\mathbf{t}_{eff}$ μ**m**	ρ_1 **kg/m^3**	ρ_2 **kg/m^3**	ρ_3 **kg/m^3**
Brick D	45.36	0.98	1686.7	$1.6\rho_1$	$10.2\rho_A$
Brick A	45.36	0.97	1792.4	$1.5\rho_1$	$8.9\rho_1$

TABLE III

PARAMETERS USED TO MODEL THE BRICK D AND BRICK A MESH STRUCTURES IN FEM SIMULATIONS.

mesh structure, and the density of aluminum and oxide, ρ = 2697 kg/m^3 and ρ = 2200 kg/m^3 respectively. In our model, we use a Poisson ratio of 0.22 and an effective plate elasticity of 45.36 GPa, The elasticity is fitted to the (1,1) resonance for the brick D structure; 261.1 kHz. The density of region 1 is calculated using the region area, the effective thickness and the mass of the metal layer in that region. Region 1 is the unloaded portion of the mesh. The non-uniform mass distributed on the mesh surface arises from the fact that we isolated the mesh into four quadrants; Region 3. We also shield the polysilicon piezoresistors on the perimeter of our mesh structures with an additional oxide layer and a metal layer; region 2. Both region 2 and 3 attribute to the non-uniformity of mass on our mesh structure. The results of the FEM simulations accounting for the effect of a distributed mass on the frequency response are shown in Table IV.

For the brick D mesh, we can see that experimentally we measure a difference between the (1,3)+(3,1) mode and the (2,2) mode of 54.1 kHz. The FEM simulations predict a shift of 40.4 kHz. Also when comparing the brick D mesh to the brick A mesh, we measure a difference of 6.8 kHz for the (1,1) mode and 17.8 kHz for the (1,3)+(3,1) mode. The FEM simulations predict a shift of 1.1 kHz for the (1,1) mode and 6.8 kHz for the (1,3)+(3,1) mode. The deviation between the experimentally measured resonances and the predicted values are best explained by the fact that we are not modeling

	Brick D Mesh		**Brick A Mesh**	
Mode	**Experimental [kHz]**	**Femlab [kHz]**	**Experimental [kHz]**	**Femlab [kHz]**
(1,1)	261.1	261.1	254.3	260.0
(1,2)		603.0	496.4	595.6
(2,1)		603.7		595.6
(1,3)+(3,1)	863.5	1019.4	845.7	1012.6
(2,2)	917.6	1059.8		1021.0

TABLE IV

FEM RESULTS: DISTRIBUTED MASS LOADING

the exact geometry of our system, because of the currently impractical finite element size that would be needed for an exact solution.. However, the lumped model does predict the same trend as seen in the LDV experiments. Thus we can conclude that the spatial location of mass on the surface of the mesh structure strongly affects the frequency response of each mesh structure. The variation in structural topology on both mesh structures can account for the the experimental measured differences seen in the scanning LDV experiments.

V. CONCLUSIONS

We have characterized the frequency response of our metal-oxide MEMS mesh structures. Our resonators consist of two different structural designs, both differ in their mass and compliance, and as expected produce different frequency responses. By driving the mesh structures in either a monopole, dipole, or quadrupole mode, we can excite high order resonant frequencies. Using a FEM simulation, the frequency response of the mesh structures are best predicted by a plate model with a distributed mass loading. We are currently investigating methods to coat the resonator with a polystyrene layer, followed by the immobilization of receptor molecules needed to detect target analytes. These steps will transform our MEMS resonator into a biosensing device.

REFERENCES

[1] M. Álvarez, L.G. Carrasocosa, M. Moreno, A. Calle, A. Zaballos, L.M. Lechuga, C. Martinez-A, and J. Tamayo. Nanomechanics of the formation of DNA self-assembled monolayers and hybridization on microcantilevers. *Langmuir*, 20:9663–9668, 2004.

[2] R. Blevins. *Formulas for natural frequency and mode shape*. Krieger, 1979.

[3] G.A. Campbell and R. Mutharasan. Detection of pathogen *Escherichia coli* O157:H7 using self-excited PZT-glass microcantilevers. *Biosenors and Bioelectronics*, 21:462–473, 2005.

[4] G.K. Fedder, S. Santhanam, M.L. Reed, S.C. Eagle, D.F. Guillou, M.S.-C. Lu, and L.R. Carley. Laminated high-aspect-ratio microstructures in a conventional CMOS process. *Sensors & Actuators A*, 57(2):103–110, November 1996.

[5] J. Grate, S. Martin, and R. White. Acoustic wave microsensors: Part I. *Analytical Chemistry*, 65(21):940–948, Nov 1993.

[6] J.J. Neumann and K.J. Gabriel. CMOS-MEMS Membrane for audio-frequency acoustic actuation. *Sensors and Actuators A*, 95:175–182, 2002.

[7] Inc. Polytec. http://www.polytec.com.

[8] S. Snellings, J. Fuller, M. Pitner, and D.W. Paul. An acoustic wave biosensor for human low-density lipoprotein particles: Construction of selective coatings. *Biosensors and Bioelectronics*, 19:353–363, 2003.

[9] Inc. The Mathworks. COMSOL - Finite Element Modeling package. http://www.comsol.com.

[10] J.E. Valentine, T.M. Przybycien, and S. Hauan. Modeling and design of a MEMS-based biosensor. Presented at the AIChE annual meeting, paper 197h, November 2003.